A High-order Sliding-Mesh Spectral Difference Method with Application to Simulation of Flows around Open Propellers

Bin Zhang[1], Roland Yu[1], Thad Michael[2] and Chunlei Liang[1*]

[1]Department of Mechanical and Aerospace Engineering, The George Washington University, USA
[2]Naval Surface Warfare Center Carderock Division, 9500 Macarthur Boulevard, West Bethesda, MD, USA

ABSTRACT

In this work, we present a high-order sliding-mesh method for simulating flows about rotating geometries. This method is based on spectral difference (SD) method and dynamic curved mortar element method. Through numerical tests, we show that this method preserves the high-order accuracy of the SD method, and is able to deal with complex rotating unstructured meshes. To further demonstrate the solver's capability, we apply it to study flow around rotating open propellers at moderate Reynolds numbers.

Keywords

high-order methods, sliding mesh, spectral difference, marine propeller.

1 INTRODUCTION

The flow around marine propellers is complicated by abundant vortical flow structures of widely varying spatial and temporal scales presenting a difficult problem for time-accurate eddy-resolving flow solvers. Furthermore, the complex geometries of marine propellers often reduce accuracy in meshing and numerical discretization. Propeller flows may also include cavitation to further complicate the problem (Chesnakas & Jessup 2003). It has become imperative to seek improved computational efficiencies in next-generation numerical solvers for very large-scale parallel simulations.

In recent years, we have developed novel high-order and highly efficient sliding-mesh spectral difference methods for simulating flows about 2D and 3D rotating geometries (Zhang & Liang 2015, Zhang et al 2016, Zhang & Liang 2016) to address these problems. Very recently, we have further pushed this method to higher orders of accuracy in both time and space for two dimensional problems (Zhang & Liang 2018).

The aim of this work is to present our recent progress on this method in three-dimensions, and application of it to preliminary studies of flow around open marine propellers. This work serves as a necessary step before further development of the solver to deal with cavitating flows around a propeller.

*Corresponding author, email: chliang@gwu.edu

2 NUMERICAL METHODS

We solve the three-dimensional compressible Navier-Stokes equations in the following conservative form

$$\frac{\partial \mathbf{Q}}{\partial t} + \frac{\partial \mathbf{F}}{\partial x} + \frac{\partial \mathbf{G}}{\partial y} + \frac{\partial \mathbf{H}}{\partial z} = 0, \tag{1}$$

where $\mathbf{Q} = [\rho\ \rho u\ \rho v\ \rho w\ E]^T$ is the vector of conservative variables, $\mathbf{F}$, $\mathbf{G}$ and $\mathbf{H}$ are the flux vectors. To study flows on rotating domains, we rewrite this equation to the arbitrary Lagrange-Eulerian (ALE) form by coordinate transformation,

$$\frac{\partial \widetilde{\mathbf{Q}}}{\partial t} + \frac{\partial \widetilde{\mathbf{F}}}{\partial \xi} + \frac{\partial \widetilde{\mathbf{G}}}{\partial \eta} + \frac{\partial \widetilde{\mathbf{H}}}{\partial \zeta} = 0, \tag{2}$$

where (ξ, η, ζ) represents the computational space, $\widetilde{\mathbf{Q}}$, $\widetilde{\mathbf{F}}$, $\widetilde{\mathbf{G}}$ and $\widetilde{\mathbf{H}}$ are the vectors of computational variables and fluxes that are related to the physical ones as: $\widetilde{\mathbf{Q}} = |J|\mathbf{Q}$, $(\widetilde{\mathbf{F}}, \widetilde{\mathbf{G}}, \widetilde{\mathbf{H}}) = |J|J^{-1}(\mathbf{F}, \mathbf{G}, \mathbf{H})$, with J denoting the Jacobian matrix for the transformation.

We solve Eq.(2) using the spectral difference (SD) method (Kopriva 1996a, 1996b; Liu, et al. 2006). In the SD method, solutions and fluxes are represented by tensor-product polynomials within each grid element,

$$\widetilde{\mathbf{Q}} = \sum_{k=1}^{N}\sum_{j=1}^{N}\sum_{i=1}^{N} \widetilde{\mathbf{Q}}_{i,j,k} h_i(\xi) h_j(\eta) h_k(\zeta), \tag{3}$$

$$\widetilde{\mathbf{F}} = \sum_{k=1}^{N}\sum_{j=1}^{N}\sum_{i=0}^{N} \widetilde{\mathbf{F}}_{i+\frac{1}{2},j,k} l_{i+\frac{1}{2}}(\xi) h_j(\eta) h_k(\zeta), \tag{4}$$

$$\widetilde{\mathbf{G}} = \sum_{k=1}^{N}\sum_{j=0}^{N}\sum_{i=1}^{N} \widetilde{\mathbf{G}}_{i,j+\frac{1}{2},k} h_i(\xi) l_{j+\frac{1}{2}}(\eta) h_k(\zeta), \tag{5}$$

$$\widetilde{\mathbf{H}} = \sum_{k=0}^{N}\sum_{j=1}^{N}\sum_{i=1}^{N} \widetilde{\mathbf{H}}_{i,j,k+\frac{1}{2}} h_i(\xi) h_j(\eta) l_{k+\frac{1}{2}}(\zeta), \tag{6}$$

where

$$h_i(X) = \prod_{s=1, s\neq i}^{N} \left(\frac{X - X_s}{X_i - X_s}\right), \text{ and} \tag{7}$$

$$l_{i+1/2}(X) = \prod_{s=0, s\neq i}^{N} \left(\frac{X - X_{s+1/2}}{X_{i+1/2} - X_{s+1/2}}\right) \tag{8}$$

are the Lagrange interpolation bases at each solution point and each flux point, respectively.

To deal with rotating objects, we split a computational domain into non-overlapping subdomains. A subdomain can enclose a rotating object and can have relative rotating motion with respect to its neighbor, resulting in non-conforming sliding interfaces in between. To account for this discontinuity in space, we use a dynamic curved mortar approach (Zhang & Liang 2015) for communication between the two sides of a sliding interface. Fig. 1 shows a schematic of the distribution of mortars between two subdomains.

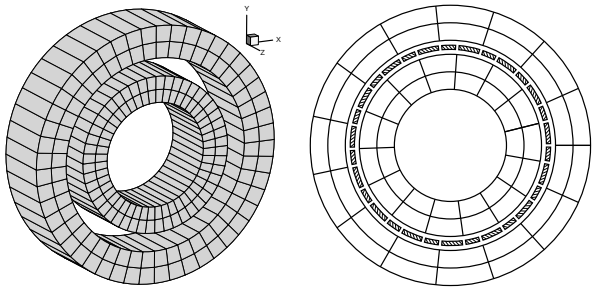

Figure 1: Schematic of distribution of mortar elements between two subdomains (inner subdomain has been scaled).

In this approach, we first map each curved grid element and mortar element to standard cube and square elements, respectively. Transfinite mapping, which can represent a circular cell face exactly, is adopted for this purpose. Subsequently, we project solutions from cell faces onto mortars to compute common solutions and common fluxes. The following least-squares projection is used for this purpose,

$$\int_0^1 \left(\mathbf{Q}^{\Xi,L}(\xi',\eta') - \mathbf{Q}^{\Omega}(\xi,\eta)\right) h_\alpha(\xi') h_\beta(\eta') d\xi' d\eta' = 0, \quad \forall \alpha,\beta = 1,2,...,N, \tag{9}$$

where $\mathbf{Q}^{\Xi,L}$ is the solution polynomial on the left side of mortar Ξ, $\mathbf{Q}^{\Omega}$ is the solution polynomial on cell face Ω, ξ' and η' represent the mortar space.

The common inviscid fluxes on mortars are computed using a Riemann solver, and are then projected back to cell faces according to

$$\int_0^{o_2}\int_0^1 (\widetilde{\mathbf{F}}^{\Omega}_{inv}(\xi,\eta) - \widetilde{\mathbf{F}}^{\Xi_1}_{inv}(\xi',\eta')) h_\alpha(\xi) h_\beta(\eta) d\xi d\eta + \int_{o_2}^1\int_0^1 (\widetilde{\mathbf{F}}^{\Omega}_{inv}(\xi,\eta) - \widetilde{\mathbf{F}}^{\Xi_2}_{inv}(\xi',\eta')) h_\alpha(\xi) h_\beta(\eta) d\xi d\eta = 0, \quad \forall \alpha,\beta = 1,2,...,N, \tag{10}$$

where $\widetilde{\mathbf{F}}^{\Xi_1}_{inv}$ and $\widetilde{\mathbf{F}}^{\Xi_2}_{inv}$ are the flux polynomials on the two mortars associated with cell face Ω, and $\widetilde{\mathbf{F}}^{\Omega}_{inv}$ is the unknown common flux polynomial on cell face Ω. The viscous fluxes are projected from cell faces to mortars in the same way as in Eq. (9), and common viscous fluxes are computed as the average of the left and the right values. The common fluxes are finally projected back to cell faces following Eq. (10).

It is provable that these projections ensure conservation, free-stream preservation, and spatial high-order accuracy (Zhang & Liang 2019). Meanwhile, the use of the exact transfinite mapping minimizes geometric errors on nonconforming sliding interfaces, which is essential for high-order time-marching accuracy (Zhang & Liang 2019).

3 NUMERICAL TESTS

3.1 Euler vortex flow

In Euler vortex flow, an isentropic vortex is superimposed to and convected by a uniform background flow. The flow field at a time instant can be analytically described as

$$u = U_\infty \left\{ \cos\theta - \frac{\epsilon y_r}{r_c} \exp\left(\frac{1 - x_r^2 - y_r^2}{2r_c^2}\right) \right\}, \tag{1}$$

$$v = U_\infty \left\{ \sin\theta + \frac{\epsilon x_r}{r_c} \exp\left(\frac{1 - x_r^2 - y_r^2}{2r_c^2}\right) \right\}, \tag{2}$$

$$\rho = \rho_\infty \left\{ 1 - \frac{(\gamma-1)(\epsilon M_\infty)^2}{2} \exp\left(\frac{1 - x_r^2 - y_r^2}{r_c^2}\right) \right\}^{\frac{1}{\gamma-1}}, \tag{3}$$

$$p = p_\infty \left\{ 1 - \frac{(\gamma-1)(\epsilon M_\infty)^2}{2} \exp\left(\frac{1 - x_r^2 - y_r^2}{r_c^2}\right) \right\}^{\frac{\gamma}{\gamma-1}}. \tag{4}$$

In the present simulation, we have: $(U_\infty, \rho_\infty) = (1,1)$, $M_\infty = 0.3$, $\epsilon = 1$, $r_c = 1$, $\theta = \arctan(1/2)$, $0 \le x, y \le 10$, and $(x_0, y_0) = (5,5)$. Fig. 2 show the mesh and an instantaneous flow field for this simulation, where the red lines represent processor interfaces. It is seen that the nonconforming sliding interface does not introduce any visible disturbance to the flow field at all.

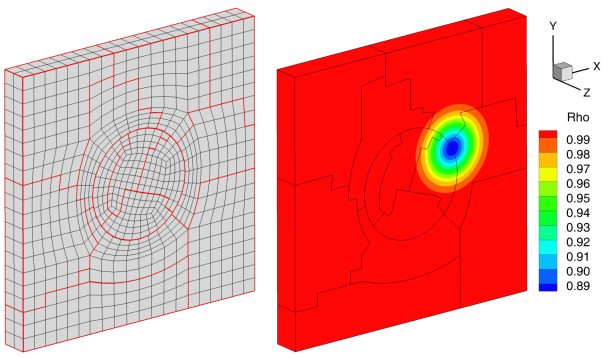

Figure 2: Mesh and density contours for the Euler vortex flow simulation.

The accuracy of the methods are evaluated by comparing the errors between the numerical solution and the analytical solution. The results are plotted in Fig. 3. We see that all three types of errors decrease exponen-

tially with the scheme order, and the method achieves the 2nd to the 10th orders without any problem.

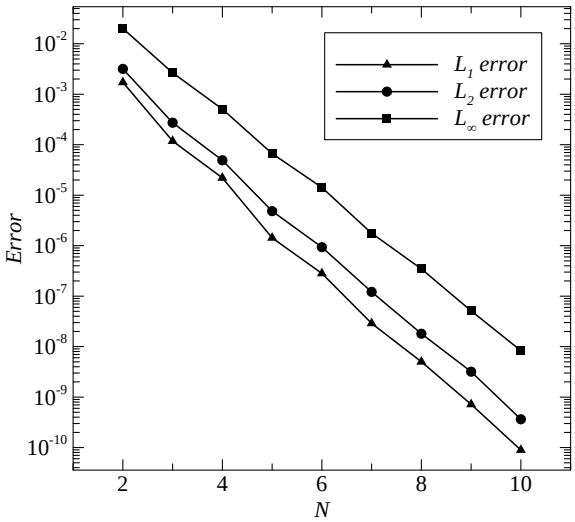

Figure 3: Orders of accuracy on Euler vortex flow.

3.2 Taylor-Couette flow

Taylor-Couette flow is formed between to concentric cylinders, with one or both of them rotating. The steady state flow has an analytical solution:

$$v_\theta = \omega_i r_i \frac{r_o/r - r/r_o}{r_o/r_i - r_i/r_o} + \omega_o r_o \frac{r/r_i - r_i/r}{r_o/r_i - r_i/r_o}. \quad (5)$$

In the present simulation, we have $r_i = 1$, $r_o = 2$, $\omega_i = 1$, $\omega_o = 0$, and $Re_i = 10$. Fig. 4 shows the meshes and the contours for this simulation, where

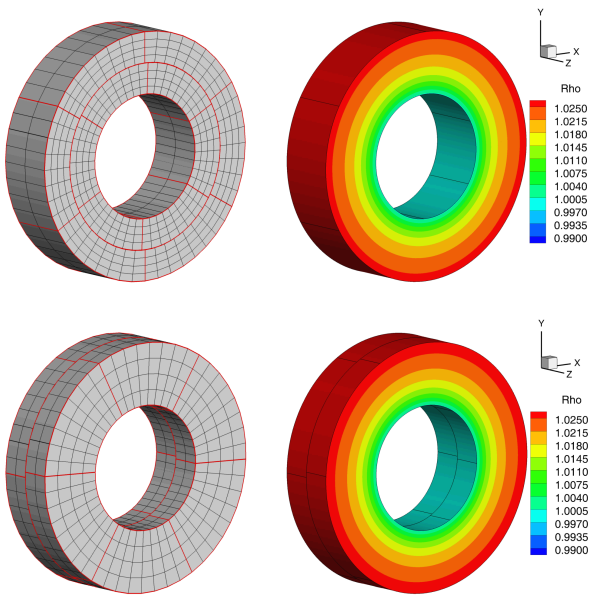

Figure 4: Mesh and steady state contours for the Taylor-Couette flow simulation with two types of sliding interfaces.

there are two types of sliding interfaces: one is along the axis, the other is perpendicular to the axis. For both cases, we see that the flow field are captured correctly.

The orders of accuracy are plotted in Fig. 5. We see that, for this viscous flow, the method also gives the optimum orders of accuracy, and we are able to achieve the 2nd to the 10th orders without any problem.

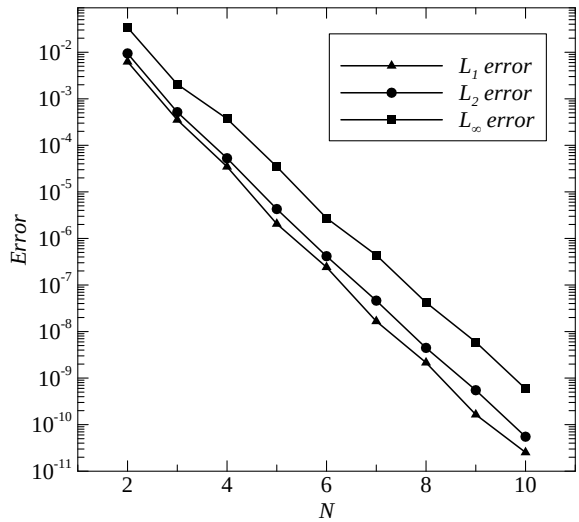

Figure 5: Orders of accuracy for the Taylor-Couette flow simulation.

4 PROPELLER SIMULATIONS

4.1 Simplified propeller

To demonstrate the capability of the method, we first apply the solver to a simplified propeller as shown in Fig. 6. The angular speed of the propeller is $\omega D/U_\infty = 0.5\pi$, and the Reynolds number of the flow is $Re = 1000$. The incoming flow has a Mach number of 0.1. The mesh has about 140,000 cells, and the simulation was performed with a fourth-order spatial and a fourth-order temporal schemes.

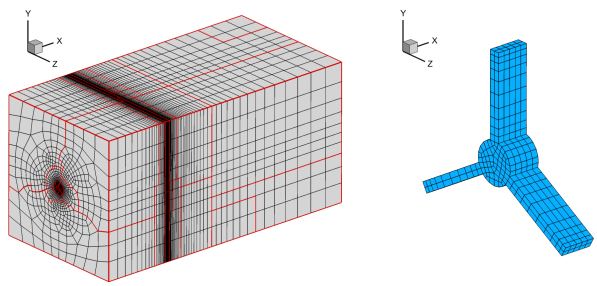

Figure 6: Mesh for the simulation of flow over a simplified propeller.

Fig. 7 shows the isosurfaces of vorticity at two time instants. It is seen that, even on a very coarse mesh, the solver is able to capture the flow structures very

well, and the flow field shows helical flow structures around the tip of each blade.

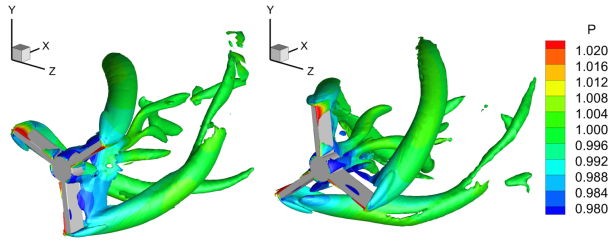

Figure 7: Isosurfaces of vorticity for flow over a simplified propeller.

A excellent capability of this method is that it can easily handle multiple rotating objects simultaneously. As an example, we apply the solver to two side-by-side propellers each of them having similar configuration as the above single propeller. And an instantaneous flow field is shown in Fig. 9

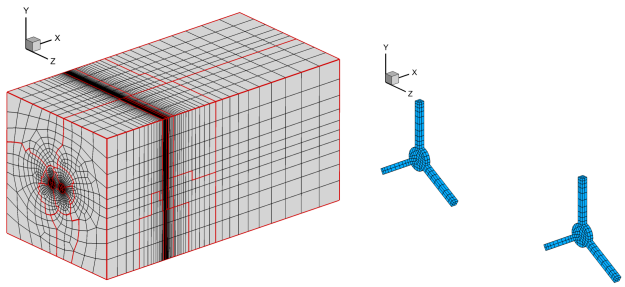

Figure 8: Mesh for the simulation of flow over two side-by-side propellers.

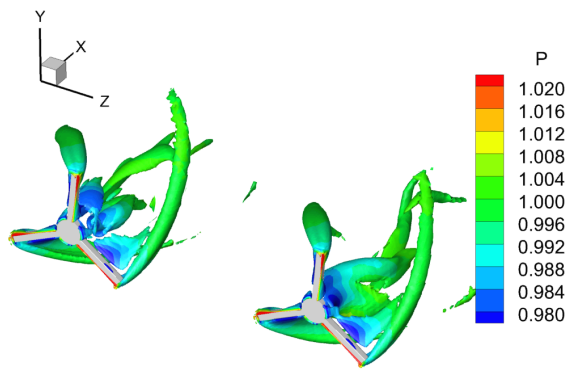

Figure 9: Isosurfaces of vorticity for flow over two side-by-side propellers.

4.2 The P4119 propeller

As a final example, we apply the solver to the P4119 marine propeller that was extensively studied in the past (e.g., (Jessup, et al. 1984)). Fig. 10 shows two views of the geometry of this three-bladed propeller.

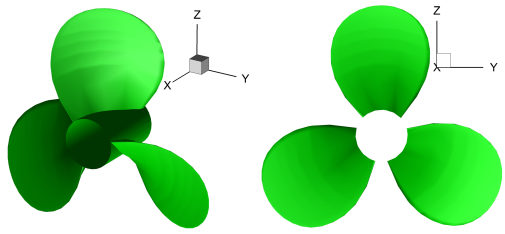

Figure 10: Geometry of the P4119 propeller.

Instead of using just one sliding interface, we employ three sliding interfaces of the two types for this simulation. Fig. 11 shows the computational domain and the meshes. The propeller is located inside a rotating disk, and this disk rotates with three sliding interfaces. The overall domain is discretized into about $80,000$ grid elements, and high-order curved elements are used along all curved boundaries. The fifth-order scheme is used for the simulation.

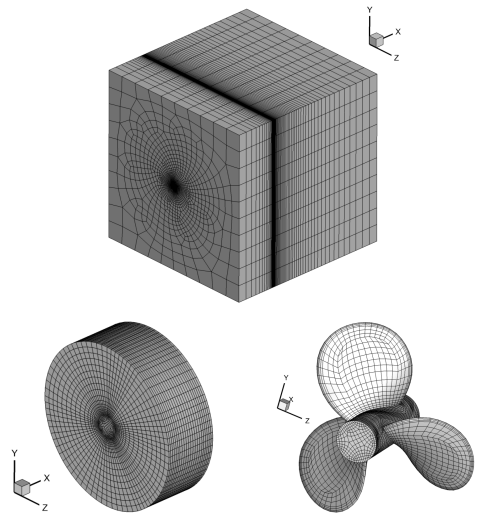

Figure 11: Mesh for the P4119 propeller simulation.

The incoming freestream flow has a Mach number of 0.1. The Reynolds number based on the freestream flow properties and the propeller diameter is $Re = 1000$. An instantaneous flow field is shown in Fig. 12. We see that the solver captures the flow structures nicely on such a coarse mesh.

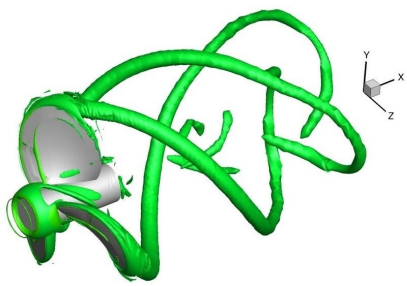

Figure 12: Instantaneous vorticity isosurface of flow over the P4119 propeller.

5 CONCLUSION

We have successfully developed a high-order sliding-mesh spectral difference method for simulating flows around three-dimensional rotating geometries. Numerical tests on both inviscid and viscous flows confirm that the method maintains the high-order accuracy of the SD method even up to very high orders. Preliminary simulation results further demonstrated the solver's capability to deal with complex geometries, such as marine propellers. These inspiring results enable us to perform large scale quantitative simulations of high-Reynolds number turbulent flows around marine propellers in the near future.

REFERENCES

Chesnakas, C. J., Jessup S. D. (2003) 'Tip-vortex Induced Cavitation on a Ducted Propulsor' Fourth ASME JSME Joint Fluids Engineering Conference.

Zhang, B., Liang, C. (2015) 'A simple, efficient, and high-order accurate curved sliding-mesh interface approach to spectral difference method on coupled rotating and stationary domains' Journal of Computational Physics **295**, pp. 147–160.

Zhang, B., Liang, C., Yang, J., Rong, Y. (2016) 'A 2D Parallel High-order Sliding and Deforming Spectral Difference Method' Computers & Fluids **139**, pp. 184–196.

Zhang, B., Liang, C. (2016) 'A High-Order Sliding-Mesh Spectral Difference Solver for Simulating Unsteady Flows around Rotating Objects' 31st Symposium on Naval Hydrodynamics, CA, USA.

Zhang, B., Qiu, Z., Liang, C. (2018) 'A flux reconstruction method with nonuniform sliding-mesh interfaces for simulating rotating flows' AIAA Paper.

Zhang, B., Liang, C. (2019) 'A parallel, conservative, space and time high-order accurate spectral difference solver for the 3D Navier-Stokes equations on sliding meshes' to be submitted.

Kopriva, D. A., Kolia J. H. (1996a) 'A conservative staggered-grid Chebyshev multidomain method for compressible flows' Journal of Computational Physics **125**, pp. 244–261.

Kopriva, D. A. (1996b) 'A conservative staggered-grid Chebyshev multidomain method for compressible flows. II. A semi-structured method' Journal of Computational Physics **128**, pp. 475–488.

Liu, Y., Vinokur M., Wang, Z. J. (2006) 'Spectral difference method for unstructured grids I: Basic formulation' Journal of Computational Physics **216**, pp. 780–801.

Jessup, S. D., Schott, C., Jeffers, M., Kobayashi, S. (1984) 'Local Propeller Blade Flows in Uniform and Sheared Onset Flows Using LDV Techniques' Fifteenth Symposium on Naval Hydrodynamics, Hamburg, Germany, pp. 221–235.